

See discussions, stats, and author profiles for this publication at: <https://www.researchgate.net/publication/259766933>

The nature of coherences in the B820 bacteriochlorophyll dimer revealed by two-dimensional electronic spectroscopy

ARTICLE *in* PHYSICAL CHEMISTRY CHEMICAL PHYSICS · JANUARY 2014

Impact Factor: 4.49 · DOI: 10.1039/c3cp54634a · Source: PubMed

CITATIONS

10

READS

110

7 AUTHORS, INCLUDING:



Marco Ferretti

VU University Amsterdam

7 PUBLICATIONS 74 CITATIONS

SEE PROFILE



Elisabet Romero

VU University Amsterdam

17 PUBLICATIONS 264 CITATIONS

SEE PROFILE



Anjali Pandit

Leiden University

28 PUBLICATIONS 273 CITATIONS

SEE PROFILE



Rienk van Grondelle

VU University Amsterdam

647 PUBLICATIONS 23,551 CITATIONS

SEE PROFILE

The nature of coherences in the B820 bacteriochlorophyll dimer revealed by two-dimensional electronic spectroscopy†

Cite this: DOI: 10.1039/c3cp54634a

Marco Ferretti,^{a*} Vladimir I. Novoderezhkin,^b Elisabet Romero,^a Ramunas Augulis,^{‡c} Anjali Pandit,^a Donatas Zigmantas^c and Rienk van Grondelle^{*a}

Light-harvesting in photosynthesis is determined by the excitonic interactions in disordered antennae and the coupling of collective electronic excitations to fast nuclear motions, producing efficient energy transfer with a complicated interplay between exciton and vibrational coherences. Two-dimensional electronic spectroscopy (2DES) is a powerful tool to study the presence of these coherences in photosynthetic complexes. However, the unambiguous assignment of the nature of the observed coherences is still under debate. In this paper we apply 2DES to an excitonically coupled bacteriochlorophyll dimer, the B820 subunit of the light harvesting complex 1 (LH1-RC) of *R. rubrum* G9. Fourier analysis of the measured kinetics and modeling of the spectral responses in a complete basis of electronic and vibrational states allow us to distinguish between pure vibrational, mixed exciton-vibrational (vibronic), and predominantly exciton coherences. The mixed coherences have been found in a wide range of oscillation frequencies, whereas exciton coherences give the biggest contributions for the frequencies in the 400–550 cm⁻¹ range, corresponding to the exciton splitting energy of the B820 dimer. Significant exciton coherences are also present at higher frequencies, *i.e.*, up to 800 cm⁻¹, which are determined by realizations of the disorder with a large energy gap between the two pigments (which increases the apparent value of the exciton splitting). Although the B820 dimer is a model system, the approach presented here represents a basis for further analyses of more complicated systems, providing a tool for studying the interplay between electronic and vibrational coherences in disordered photosynthetic antennae and reaction centres.

Received 1st November 2013,
Accepted 16th December 2013

DOI: 10.1039/c3cp54634a

www.rsc.org/pccp

1 Introduction

The success of natural photosynthesis is based on two ultrafast processes: excitation energy transfer after light absorption by the photosynthetic light harvesting antenna followed by transmembrane charge separation in the photosynthetic reaction centre.^{1–3} Both processes occur with a quantum efficiency approaching unity in spite of the highly disordered nature of these biological systems. In recent years, the role of quantum mechanics, disorder and coherence^{4–7} has been proposed to explain the high energy conversion efficiency of the primary steps of photosynthesis.

Two-dimensional electronic spectroscopy (2DES) is a tool to study the presence and the role of quantum coherences in biological complexes.^{8–10} In this technique three spectrally broad and ultra-short laser pulses are used to set and detect the coherent superposition of quantum states in the complex. The three pulses are time delayed, and fast Fourier transformation (FFT) with respect to the coherence time τ (the time between the first and the second pulse) and with respect to the rephasing time t (the time between the third pulse and the emitted signal) results in 2D spectra which correlate the absorbed frequency ω_τ with the emitted frequency ω_t for a fixed population time T (the time between the second and the third pulse). The population time dynamics is related to the evolution of quantum coherence between quantum states and to energy transfer. The coherence appears as peak amplitude oscillations during T , whereas energy transfer appears as non-oscillating crosspeaks. Although originally off-diagonal amplitude oscillations were associated with exciton coherence¹⁰ and diagonal amplitude oscillations with vibrational coherences, recently, electronic-vibrational (vibronic) models, with both diagonal and off-diagonal contributions

^a VU University, Amsterdam, The Netherlands. E-mail: m.ferretti@vu.nl^b A.N. Belozersky Institute of Physico-Chemical Biology, Moscow State University, Leninskie Gory, 119992, Moscow, Russia^c Lund University, Lund, Sweden

† Electronic supplementary information (ESI) available. See DOI: 10.1039/c3cp54634a

‡ Present address: Center for Physical Science and Technology, Vilnius, Lithuania.

to the oscillations, have been proposed.^{11–15} Within the proposed mechanism, vibronic coherences appear when the exciton splitting energy is resonant with vibrational modes, and this resonance is potentially able to sustain, regenerate, or even (re-)create coherences between electronic states during the time scale of energy and electron transfer.^{11,12,14,16–18} However, due to the complexity of the exciton manifold of most of the photosynthetic complexes, the nature of the observed coherences has not been unambiguously determined yet. The B820 pigment–protein complex is a good candidate for testing the technique and the theoretical models describing coherence in biology due to its simple exciton manifold. The B820 subunit consists of a protein-bound bacteriochlorophyll (BChl) dimer which is the basic building block of the light-harvesting 1 (LH1) pigment–protein complex from purple bacteria.^{19–21} This pigment–protein subunit consists of a heterodimer of one α and one β polypeptide which non-covalently binds the two BChl pigments.²² The B820 dimer exciton manifold is described by four exciton states: one ground state, two one-exciton states absorbing at 795 nm and 820 nm, and one double exciton state (Fig. 1). The exciton state at 795 nm is almost dark and it appears as a shoulder in the steady state absorption spectrum whereas the exciton state at 820 nm is super-radiant²² (Fig. 1). The exciton splitting energy of the B820 dimer ($400\text{--}500\text{ cm}^{-1}$) is comparable to the frequencies of the most dominant intramolecular BChl vibrational modes (as observed in a transient absorption experiment on mutants of the bacterial reaction center²³). Moreover, the absorption intensity of the higher energy exciton component is of the same

order of magnitude as the intensities of the vibrational satellites in the blue wing of the absorption in this complex. Thus, the B820 is an excellent model system to investigate the interplay between exciton and vibrational coherences. The energetic disorder in B820, caused by slow protein motions (with respect to the ultrafast dynamics probed by 2DES), is large enough^{24–26} to create a spread of the apparent exciton splitting from 400 to 800 cm^{-1} , which can become resonant with the most intense vibrational modes.

Here, we have measured the 2D spectra of B820 at room temperature and studied the population time dynamics, in order to understand the nature of the coherences. A Fourier transformation with respect to the population time T is applied in order to select only those spectral features oscillating with particular frequencies during the population time. The amplitude oscillations reflect quantum coherences within the system which can have exciton, vibrational or vibronic origins. We have applied a model based on a two-pigment Hamiltonian in the complete diabatic basis of electronic and vibrational states to calculate the linear and non-linear (2D) spectral responses. The model enables us to explore the interplay between exciton and vibrational coherences for a single realization of the disorder, and to reproduce the experimentally obtained disorder-averaged 2D frequency maps. We find the simultaneous presence of exciton and vibrational coherence and estimate the degree of exciton-vibrational mixing.

2 Experimental results

2D electronic spectra

The 2D real rephasing spectra, for T equal to 20, 100, 220 and 500 fs, are shown in Fig. 2. The signal along the diagonal is dominated by a positive band at 815 nm which corresponds to the contributions of ground state bleach (GSB) and stimulated emission (SE) from the 820 nm super-radiant state. The almost-dark state at 795 nm is undistinguishable in the 2D spectra in agreement with its low amplitude in the steady state absorption spectrum shown in Fig. 1. The off-diagonal peaks are both

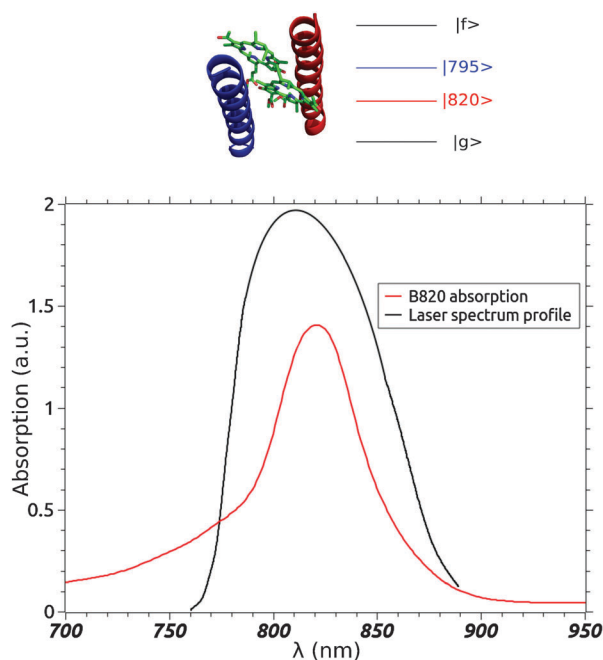


Fig. 1 Top left frame: expected pigment–protein arrangement of the B820 subunit adapted from the crystal structure of the reaction center light-harvesting complex 1 of *Rhodospseudomonas palustris*.²³ Top right frame: the B820 exciton energy level scheme without vibrational coupling. Bottom frame: the B820 room temperature steady-state absorption spectrum and the laser spectral profile.

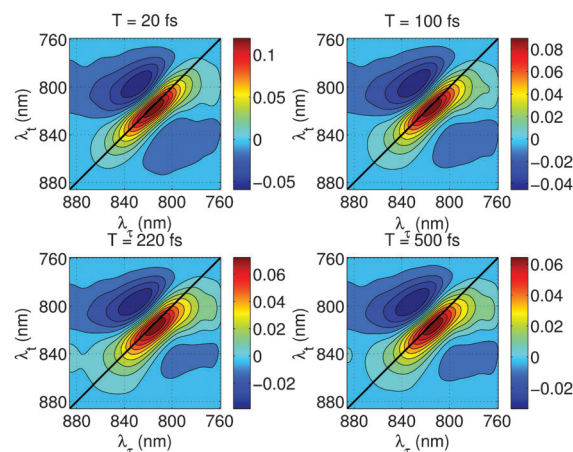


Fig. 2 2D real rephasing spectra at population time (T) equal to 20, 100, 220 and 500 fs at room temperature.

negative and correspond to the intrinsic lineshape of the rephasing 2D spectrum and to the excited state absorption (ESA). The (superposition) states created by the three laser pulses and their rephasing can be described by double-sided Feynman diagrams. These diagrams allow us to assign certain processes to specific locations (λ_τ , λ_t) in the 2D spectra. With the Feynman diagrams (see ESI†) it is possible to show that the peak at ($\lambda_\tau = 830$ nm, $\lambda_t = 795$ nm) corresponds to the excitation from the one-exciton 820 nm state to the double-exciton f state (where both monomers are excited), whereas the peak at (804 nm, 845 nm) corresponds to an excitation from the 795 nm state to the f state (see ESI† for 2D total real spectrum).

2D traces and quantum beats

The 2D traces (Fig. 3, top frame), the real rephasing amplitude as a function of population time T , are analyzed in order to study the dynamic evolution of the spectra. The traces show a bi-exponential decay modulated by oscillations. The origin of the multi-exponential decay is due to several relaxation processes, which occur on different time scales, *e.g.* excitonic

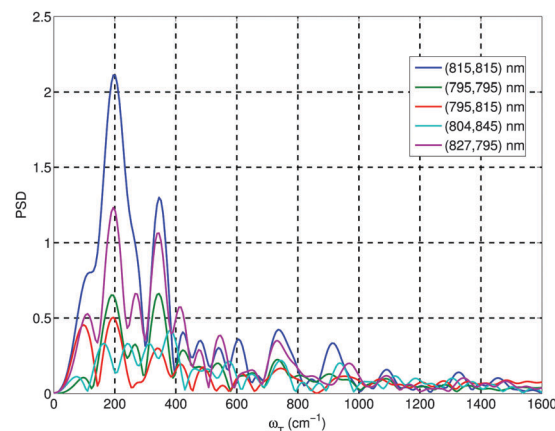


Fig. 4 Power spectral density of the quantum beats indicating the different oscillation frequencies of the system. For a list of the most prominent frequencies see Table 1.

Table 1 Oscillation frequencies of the 2D real rephasing spectra obtained by Fourier analysis of residues in Fig. 2. Almost all of them were previously measured by transient absorption (TA)³⁴ or by 3 pulse echo peak shift (3PEPS)³⁵

ω_T (cm ⁻¹)	TA	3PEPS
68	X	
120		X
192		X
270		
340	X	
440	X	
553		X
745	X	X

relaxation in hundreds of femtoseconds and vibrational relaxation in a few picoseconds.²⁷ The presence of amplitude oscillations, the so called quantum beats, is a signature of quantum coherence. The traces are fitted with a bi-exponential decay which is then subtracted from the original traces. The resulting residues, which are the quantum beats, are shown in Fig. 3 (bottom frame). A fast Fourier transformation (FFT) is applied to the residues in order to evaluate the oscillation frequencies contained in the quantum beats. The power spectral density (PSD) of the FFT is shown in Fig. 4 and the corresponding frequencies are reported in Table 1. For the interpretation of the frequencies and the nature of the coherences see the *modelling of 2D frequency maps* section below.

2D real rephasing frequency maps

The analysis of the 2D traces presented in the previous section is applied to the whole 2D spectrum, *i.e.*, to all the different (λ_τ , λ_t) combinations. The result is represented by 2D frequency maps, each of them corresponding to different ω_T frequencies, instead of being associated with different time T (as is the case for the 2D spectra). These maps show only the state superpositions which oscillate with a certain frequency ω_T during T . Four maps corresponding to ω_T equal to 345, 416, 546 and 735 cm⁻¹ are shown in Fig. 5. Note that the ω_T resolution is

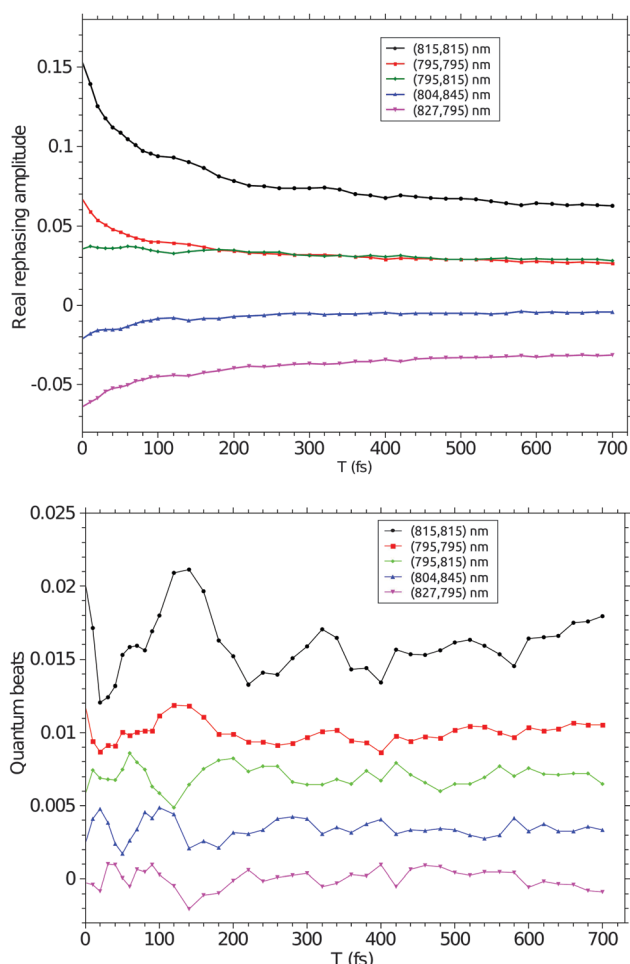


Fig. 3 Top frame: population time (T) dynamics of representative 2D real rephasing peaks. Bottom frame: quantum beats obtained after subtraction of the bi-exponential decay from the traces shown in the top frame. Some of the traces have been vertically translated for better visualization.

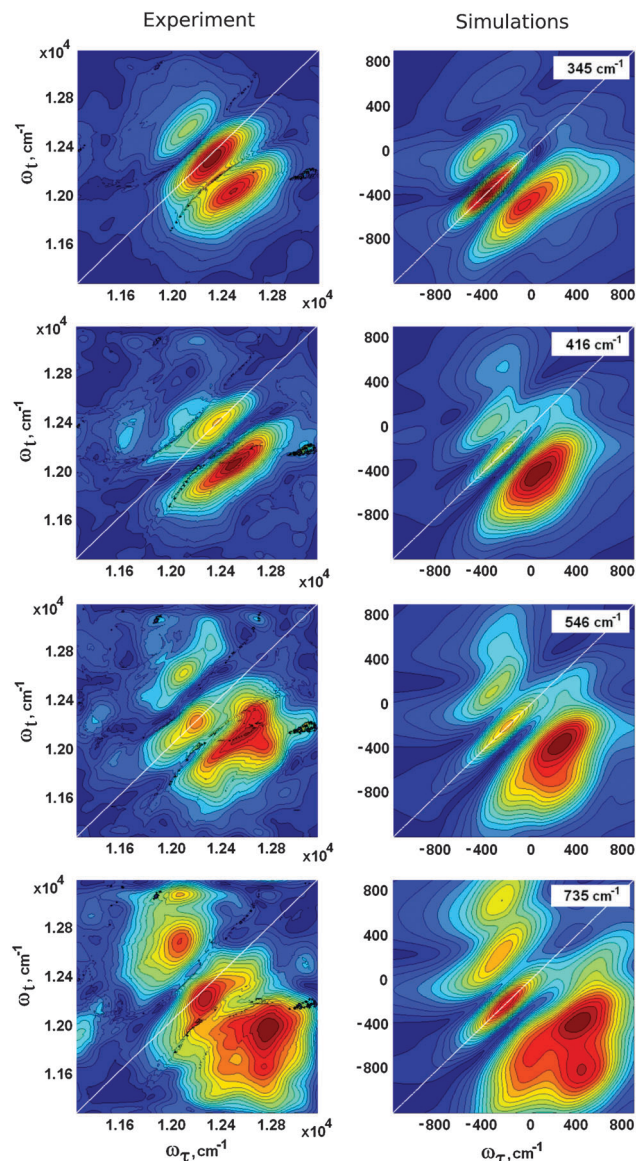


Fig. 5 B820 2D frequency maps at $\omega_T = 345, 416, 546$, and 735 cm^{-1} ; experimental (left frame) and calculated (right frame) maps. The calculation is performed at room temperature, averaging over disorder ($\sigma = 650 \text{ cm}^{-1}$) and with $\alpha = 25^\circ$ and $M_{12} = -270 \text{ cm}^{-1}$. The excited states are coupled to a single vibrational mode, taken from a specific manifold as discussed in the text. In the calculated maps the energy is counted from the unperturbed zero-phonon energies $\omega_{10} = \omega_{20}$, which correspond to the electronic excitation of a BChl monomer from the lowest vibrational level of the ground state to the lowest vibrational level of the excited state (without disorder).

about 90 cm^{-1} . The low frequency map at 345 cm^{-1} shows an intense diagonal peak at 820 nm and two weaker off-diagonal peaks at $(830, 810)$ and at $(810, 830) \text{ nm}$. In the maps corresponding to frequencies near the exciton splitting ($400\text{--}550 \text{ cm}^{-1}$) the below-diagonal peaks at $(800, 830) \text{ nm}$ becomes dominant. At higher frequencies, such as 735 cm^{-1} , the amplitudes of both diagonal and off-diagonal peaks are comparable, and the off-diagonal peaks show complicated structures. Even though the 735 cm^{-1} frequency exceeds the expected exciton splitting

energy, exciton coherence can still appear in realizations of the disorder with significant asymmetry between the two BChl molecules, for instance, realizations with an energy difference of 200 cm^{-1} between the two site energies. In this way the disorder can produce a mixed exciton-vibrational or predominantly exciton coherence at any frequency. To understand the origin of the coherences, we model the third-order response of the system in the basis of electron-vibrational eigenstates, taking into account the disorder in the site energies and the coupling of single vibrational modes to the exciton manifold of the system.

3 Modelling

Exciton-vibrational Hamiltonian

To study the interplay of electronic and vibrational coherences in the B820 dimer we use a model containing two sites (diabatic states) coupled to a single vibrational mode. The system (exciton-vibrational) Hamiltonian in the site (diabatic) representation is:

$$H_{\text{ex-vib}} = H_g + H_e + H_f$$

$$H_g = |g\rangle \left[\Omega \sum_{s=x,y} \left[\frac{1}{2} (\Delta_g^s)^2 + \left(\beta_s^+ \beta_s + \frac{1}{2} \right) - \frac{1}{\sqrt{2}} \Delta_g^s (\beta_s + \beta_s^+) \right] \right] \langle g|$$

$$H_e = \sum_{n=1,2} |n\rangle \left[\omega_{n0} + \Omega \sum_{s=x,y} \left[\frac{1}{2} (\Delta_n^s)^2 + \left(\beta_s^+ \beta_s + \frac{1}{2} \right) - \frac{1}{\sqrt{2}} \Delta_n^s (\beta_s + \beta_s^+) \right] \right] \langle n| + \sum_{n \neq m} |n\rangle M_{nm} \langle m|$$

$$H_f = |f\rangle \left[\omega_{10} + \omega_{20} + \Omega \sum_{s=x,y} \left[\frac{1}{2} (\Delta_f^s)^2 + \left(\beta_s^+ \beta_s + \frac{1}{2} \right) - \frac{1}{\sqrt{2}} \Delta_f^s (\beta_s + \beta_s^+) \right] \right] \langle f|$$

where H_g , H_e and H_f represent the Hamiltonian for none, one or both monomers excited, respectively.

The basic states are given by a direct product of the electronic wavefunctions (ground $|g\rangle$, one-exciton $|n\rangle$, two-exciton $|f\rangle$) and vibrational wavefunctions $|a_s\rangle$ depending on the effective nuclear coordinates $s = x, y$. Note that x and y do not represent spatial coordinates, but the displacement in two independent directions. The basis wavefunctions $|a_s\rangle$ are unshifted, *i.e.*, have zero displacement along the x - and y -coordinates. The creation and annihilation phonon operators β_s^+ and β_s work on this unshifted basis. The displacements of the electronic surfaces along the s -coordinates (Δ_g^s , Δ_n^s , Δ_f^s) are accounted for by the shifting operators $\Omega \Delta_s (\beta_s + \beta_s^+) / \sqrt{2}$, where Ω is the vibrational frequency. Excitation of the diabatic state n corresponds to the $g \rightarrow n$ transition with the electronic transition dipole d_n and zero-phonon transition energy ω_{n0} . The interaction between the diabatic states is given by the energy M_{12} that is supposed to be independent of the vibrational coordinates. The two-exciton manifold consists of a single state corresponding to excitation of

the two sites, *i.e.*, $|f\rangle = |1,2\rangle$. Diagonalization of the Hamiltonian gives the exciton-vibronic (vibronic) eigenstates:

$$H_g C^g = C^g E^g; \quad |c\rangle = \sum_a C_{ac}^g |g, a\rangle; \quad E_{cc'}^g = \delta_{cc'} \omega_c$$

$$H_e C^e = C^e E^e; \quad |b\rangle = \sum_{n,a} C_{n,ab}^e |n, a\rangle; \quad E_{bb'}^e = \delta_{bb'} \omega_b$$

$$H_f C^f = C^f E^f; \quad |r\rangle = \sum_a C_{ar}^f |f, a\rangle; \quad E_{rr'}^f = \delta_{rr'} \omega_r$$

where $|a\rangle = |a_x, a_y\rangle$ is the product of the vibrational wavefunctions corresponding to the *x*- and *y*-coordinates; $|g, a\rangle$, $|n, a\rangle$, and $|f, a\rangle$ denote a product of the electronic and vibrational wavefunctions. The transition dipoles between the ground, one- and two-exciton vibronic manifolds (denoted as *c*, *b*, and *r*, respectively) are:

$$d_{bc} = \sum_{n,a} C_{n,ab}^e d_n C_{ac}^g$$

$$d_{rb} = \sum_{n \neq m} C_{ar}^f (d_m C_{n,ab}^e + d_n C_{m,ab}^e)$$

Note that a similar approach has been previously employed to model electron transfer coupled to a coherent vibrational motion along two nuclear coordinates in the bacterial reaction centre,²⁸ and recently the same Hamiltonian was used to explore the structure of the electronic and vibrational coherences in the 2D spectral responses of a molecular dimer.^{15,29} In the present modelling we use displacements $\{\Delta_g^x, \Delta_g^y\} = \Delta/2\{-1, -1\}$ for the ground state $|g\rangle$; $\{\Delta_1^x, \Delta_1^y\} = \Delta/2\{1, -1\}$ and $\{\Delta_2^x, \Delta_2^y\} = \Delta/2\{-1, 1\}$ for the excited states $|1\rangle$ and $|2\rangle$; and $\{\Delta_r^x, \Delta_r^y\} = \Delta/2\{1, 1\}$ for the two-exciton state $|f\rangle = |1,2\rangle$. Note that the relative displacements for the $|1\rangle \rightarrow |1,2\rangle$ and $|2\rangle \rightarrow |1,2\rangle$ transitions are the same as for the $|g\rangle \rightarrow |2\rangle$ and $|g\rangle \rightarrow |1\rangle$ transitions, respectively. The minima of the potential surfaces of the diabatic states 1 and 2 are displaced (with respect to each other) along the *x* – *y* direction. Therefore, the nuclear motion along this direction is affected by the mixing between the diabatic states. Note that the dynamics along the *x* – *y* direction corresponds to anticorrelated nuclear motion within the states 1 and 2.

Exciton-vibronic structure of the absorption spectrum

We consider a symmetric dimer with equal unperturbed site energies $\omega_{10} = \omega_{20}$. The static disorder is modeled by uncorrelated shifts of the site energies randomly taken from a Gaussian distribution with full width at half maximum (FWHM) of $\sigma = 650 \text{ cm}^{-1}$. The interaction energy M_{12} was varied from -250 to -300 cm^{-1} . These values are close to the parameters determined from a quantitative fit of the B820 non-linear transient absorption (pump-probe) spectra.²⁴ The angle between the two transition dipoles α was varied from 0° to 30° . First, we calculate the absorption spectra of one specific realization of the disorder with the site energies $\omega_{10} - \delta\omega/2$ and $\omega_{20} + \delta\omega/2$, where $\delta\omega = 400 \text{ cm}^{-1}$. The stick absorption spectra of this specific realization coupled to three different vibrational frequencies are shown in Fig. 6. The calculation is restricted to the low-temperature limit, when transitions occur only from

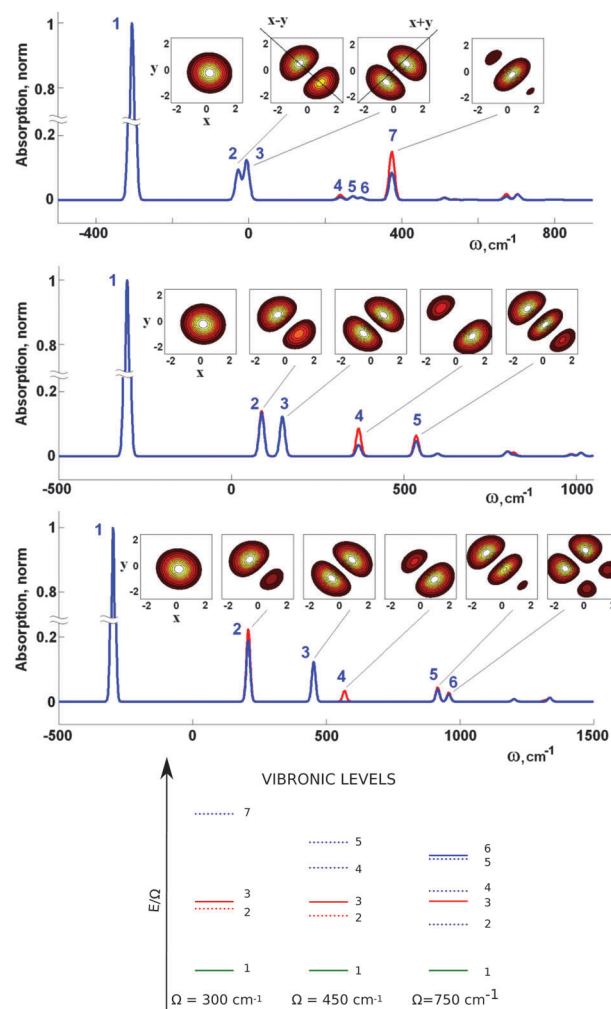


Fig. 6 Top frame: calculated absorption spectra of a dimer with $\delta\omega = 400 \text{ cm}^{-1}$ and $\Omega = 300 \text{ cm}^{-1}$ (top), 450 cm^{-1} (middle), and 750 cm^{-1} (bottom). All the spectra are normalized to unity. Blue curves correspond to parallel dipole moments ($\alpha = 0^\circ$), whereas red curves show additional components (or increase in amplitudes) appearing at $\alpha = 30^\circ$. The parameters of the model are: $M_{12} = -250 \text{ cm}^{-1}$ (both for $\alpha = 0^\circ$ and 30°), low temperature limit (only the lowest vibrational level of the ground state is populated), equal displacement $\Delta = 0.7$ for all the vibrational frequencies, and equal line-width of 10 cm^{-1} (at Hw^{-1}) for all the absorption components. The energies on the abscissa are counted from the unperturbed $\omega_{10} = \omega_{20}$ value. The insets show the shape of the wavefunctions (plotted as contour lines in the *x,y* plane) for the exciton-vibronic levels corresponding to the most intense components of the absorption spectra, *i.e.*, $b = 1, 2, 3, 7$ ($\Omega = 300 \text{ cm}^{-1}$), $b = 1-5$ ($\Omega = 450 \text{ cm}^{-1}$), and $b = 1-6$ ($\Omega = 750 \text{ cm}^{-1}$). Bottom frame: the vibronic level scheme normalized to the corresponding vibrational frequency Ω . The zero phonon line of the lower exciton component (*i.e.*, level 1) is shown in green; the first vibrational satellites of the lower exciton component (levels 2 and 3) are shown in red; the levels of the higher exciton component are shown in blue. Dashed lines refer to anticorrelated wavefunctions, whereas continuous lines to correlated ones. The pure vibrational levels (level 3) are all at the same energy (after normalization to Ω). The higher the frequency Ω , the larger the shift of the level 2 from the pure vibrational level 3. When Ω exceeds the exciton splitting ($\Omega = 750 \text{ cm}^{-1}$) the level 2 becomes predominantly excitonic (shown in blue in the $\Omega = 750 \text{ cm}^{-1}$ level diagram).

the lowest vibrational level of the ground state. As a result, the absorption components can be characterized by a single index *b* corresponding to the number of one-exciton vibronic

state (the vibronic states are numbered in increasing order of their energies).

The $\Omega = 300 \text{ cm}^{-1}$ top frame in Fig. 6 illustrates the situation when the vibrational frequency that couples to the excitonic manifold is lower than the exciton splitting ($2M_{12} = 500 \text{ cm}^{-1}$). In this case the spectrum consists of an intense zero-phonon line ($b = 1$) of the lowest exciton component accompanied by a vibrational satellite (containing two almost degenerate $b = 2, 3$ levels). The $b = 3$ level has a symmetric wavefunction (see insets in Fig. 6) with the maxima oriented along the $x + y$ direction. This direction (indicated in the inset of Fig. 6) corresponds to a correlated nuclear motion in the sites ($n = 1$ and 2), *i.e.*, motion along the $x = y$ line. The $b = 3$ level is shifted from the lowest transition exactly by Ω and the dipole strength is independent of the frequency Ω and the mutual dipole orientation α , differently from the other vibronic states. On the other hand, the second ($b = 2$) level corresponds to the ‘anticorrelated’ direction $x - y$, that is affected by the mixing of the two sites. This direction (indicated in the inset of Fig. 6) corresponds to a motion along the $x = -y$ line. In the disordered case ($\delta\omega = 400 \text{ cm}^{-1}$ in our example), the $b = 2$ wavefunctions are asymmetric reflecting exciton mixing between the sites with different energies. In addition, the mixing changes the shape of the potentials in the $x - y$ direction and produces vibronic levels with smaller splitting as compared to the original frequency Ω . At low frequencies, $\Omega \ll 2M_{12}$, the $b = 2$ and $b = 3$ levels have the same intensity and almost the same energy. Increasing the vibrational frequency Ω results in an increasingly bigger splitting between the $b = 2$ and $b = 3$ levels and increasingly larger dipole strength for the $b = 2$ level due to exciton mixing. Further to the blue from the $b = 2, 3$ pair we find the lowest vibronic state of the higher exciton component ($b = 7$) that is relatively weak (due to the small angle between the dipoles). Disorder increases the splitting between the main vibronic levels of the two exciton components ($b = 1$ and $b = 7$) and makes the higher component allowed even for $\alpha = 0^\circ$.

The $\Omega = 450 \text{ cm}^{-1}$ middle frame in Fig. 6 shows the situation when the vibrational frequency approaches the exciton splitting. In this case the anticorrelated component of the first vibrational satellite ($b = 2$) becomes more intense, more shifted from the correlated one ($b = 3$), and contains some degree of exciton mixing (depending on the angle between the dipoles as can be seen from the small, but distinguishable difference between the red and the blue curves). The upper exciton component is split into two sublevels ($b = 4$ and 5). The value of the splitting as well as the intensities of these levels increases with the disorder value $\delta\omega$. Consequently, in this case the stick absorption spectrum consists of one pure vibrational level (correlated vibrational component $b = 3$), one exciton-vibrational level (anticorrelated vibrational component $b = 2$) and two predominantly exciton components ($b = 4, 5$).

The lower frame in Fig. 6 corresponds to $\Omega = 750 \text{ cm}^{-1}$. This vibrational frequency exceeds the exciton splitting, and the order of the upper exciton and vibrational components is opposite to the low-frequency case. Close to the main zero-phonon line ($b = 1$) we find a single and predominantly exciton

level corresponding to the upper exciton component. In fact this is the anticorrelated $b = 2$ component, but strongly transformed and red-shifted due to significant exciton contribution. Other predominantly exciton components ($b = 4$ and $b = 5, 6$) are similar to the $b = 4$ and 5 levels in the $\Omega = 450 \text{ cm}^{-1}$ case, but they are less intense and more split. In this case the absorption spectrum can be treated as consisting of the lower exciton component (with the $b = 1$ origin and $b = 3$ vibrational satellite) and a higher exciton component (with the $b = 2$ origin and $b = 5, 6$ satellites, where $b = 5$ is the anticorrelated and $b = 6$ is the correlated component as can be seen from their wavefunctions). Disorder increases the splitting between these states.

Exciton and vibrational coherences in the 2D photon echo

In order to illustrate the interplay of exciton and vibrational coherences in the 2D spectra we will show the positions of the main components oscillating at a certain frequency in the 2D frequency maps. The calculation is restricted to the low-temperature limit and to coherent dynamics (*i.e.*, relaxation between exciton-vibrational components is not included). As an example we calculate the intensities of the rephasing stimulated emission (SE) components oscillating with the frequencies $\omega_{bb'} = \omega_b - \omega_{b'}$ on the $\{\omega_\tau, \omega_t\}$ plane, where $\omega_\tau = \omega_{b'0}$ is the excitation frequency (corresponding to transition from the lowest $c = 0$ level of the ground state to the exciton-vibrational level b' of the excited-state manifold) and $\omega_t = \omega_{bc}$ is the emitting frequency (emission from the excited state b to the state c of the ground state). The coherence between the b and b' states can have purely vibrational, mixed exciton-vibrational, or purely exciton origin. The degree of exciton mixing P_{coh} present in the b - b' coherence can be defined as:

$$P_{\text{coh}}(b, b') = \left| \sum_a C_{1,ab}^e C_{2,ab'}^e \right| + \left| \sum_a C_{2,ab}^e C_{1,ab'}^e \right|$$

The maximal value $P_{\text{coh}} = 1$ corresponds to a pure exciton mixing with complete delocalization over the two sites. For a purely vibrational coherence without any exciton mixing P_{coh} is equal to zero. In Fig. 7 we consider three cases with $\Omega = 300, 450$, and 750 cm^{-1} (with the same parameters as in the examples shown in Fig. 6).

In the $\Omega = 300 \text{ cm}^{-1}$ case (Fig. 7, top frame), the coherence between the $b = 1$ and $b = 3$ levels (1,3) produces four intense SE peaks oscillating with the frequency $\Omega = 300 \text{ cm}^{-1}$. The structure of this quadruplet is exactly the same as for the SE of a single electronic transition coupled to one vibrational mode. The (1,2) coherence produces a very similar quadruplet, but with a slightly different oscillation frequency, *i.e.*, 278 cm^{-1} . The (1-3) and (1-2) coherences correspond to coherent nuclear motion along correlated $x + y$ and anticorrelated $x - y$ coordinates, respectively (as can be seen from the shapes of the wavefunctions shown in Fig. 6). The degree of exciton mixing is $P_{\text{coh}}(1,3) = 0$ and $P_{\text{coh}}(1,2) = 0.17$, corresponding to a pure vibrational and a mixed exciton-vibrational coherence, respectively. The (1-7) coherence yields two intense excitonic peaks with $P_{\text{coh}}(1,7) = 0.88$ and with symmetric positions with respect to the diagonal in the 2D

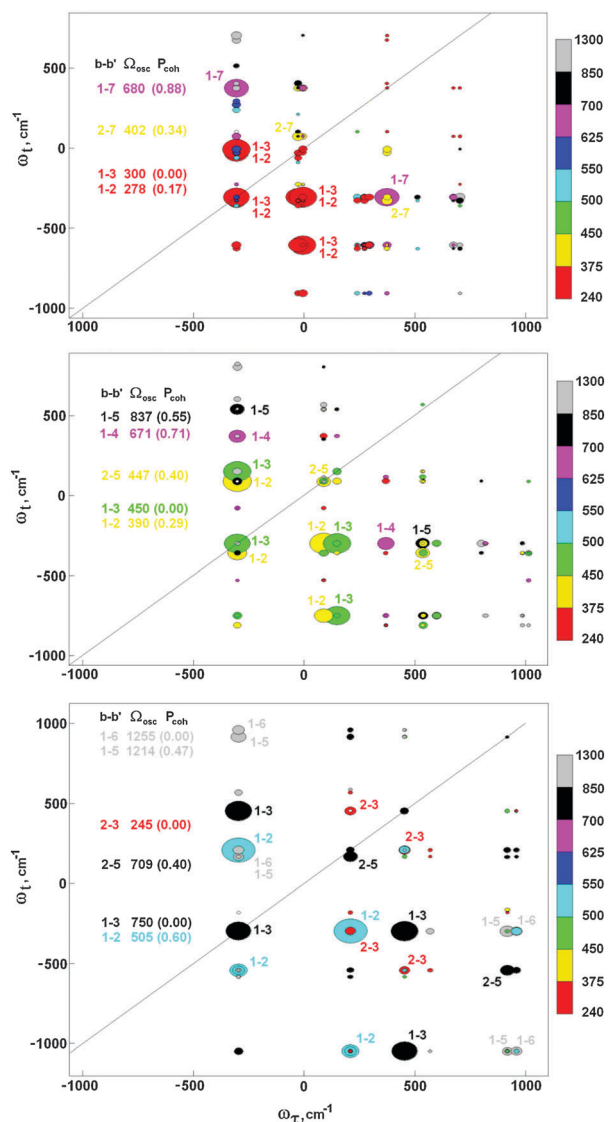


Fig. 7 Intensities of the SE components of the 2D frequency maps calculated for $\Omega = 300 \text{ cm}^{-1}$ (top), 450 cm^{-1} (middle), and 750 cm^{-1} (bottom). Other parameters are the same as in Fig. 6, *i.e.*, $\delta\omega = 400 \text{ cm}^{-1}$, $\alpha = 30^\circ$, $M_{12} = -250 \text{ cm}^{-1}$, $\Delta = 0.7$. The positions of the components are shown as a function of excitation ω_e and emission ω_t frequencies (counted from the unperturbed $\omega_{10} = \omega_{20}$ value). The area of the circles is proportional to the intensity of that component in the 2D frequency map; the colors indicate the oscillation frequency (as shown in the colorbar on the right). Parallel polarization of the four pulses and the low-temperature limit are assumed; the relaxation between the exciton-vibrational levels is neglected. The intensities are calculated with dipole orientation averaging. The numbers near the most intense components correspond to the $b-b'$ indices, specifying which pair of levels is coherently excited. On the left side we show oscillation frequencies Ω_{osc} (in cm^{-1}) and the degree of exciton mixing (P_{coh}) for these pairs.

frequency map. The oscillation frequency in this case is 680 cm^{-1} (which is significantly larger than the exciton splitting, due to the inclusion of the energy difference ($\delta\omega = 400 \text{ cm}^{-1}$) that accounts for one realization of the site energy disorder). This oscillation frequency will of course be different in other realizations of the disorder. There is also coherence between the $b = 2$ and 7 levels

with $P_{\text{coh}}(2,7) = 0.34$ and 402 cm^{-1} oscillation frequency. This duplet is not purely excitonic, has a smaller amplitude, and its position is shifted along the antidiagonal direction (*i.e.*, one peak is near the diagonal and the other is below the diagonal). Both $(1-7)$ and $(2-7)$ coherences correspond to a motion along the $x - y$ coordinate (Fig. 6).

At $\Omega = 450 \text{ cm}^{-1}$ we obtain two vibrational quadruplets $1-3$ and $1-2$ (now with a larger difference in oscillation frequencies as compared to the $\Omega = 300 \text{ cm}^{-1}$ case), two symmetric exciton duplets $1-4$ and $1-5$ (oscillating at 670 and 837 cm^{-1}), and one exciton duplet $2-5$ with antidiagonal shift (oscillating at 447 cm^{-1}). The $P_{\text{coh}}(1,2)$ value for the anticorrelated vibration has increased indicating larger exciton mixing, whereas the $P_{\text{coh}}(1,4)$ value for the most intense exciton pair is reduced. Thus, the exciton and vibrational degrees of freedom are more strongly mixed when the vibrational frequency is near the excitonic splitting.

At $\Omega = 750 \text{ cm}^{-1}$ the anticorrelated vibrational quadruplet $1-2$ becomes more excitonic than vibrational with $P_{\text{coh}}(1,2) = 0.6$ and oscillates with a frequency of 505 cm^{-1} , which is close to the exciton splitting (and far from the original 750 cm^{-1} vibration). In addition, this quadruplet becomes more intense than the purely vibrational quadruplet $1-3$. Moreover, the upper pair of the $1-2$ peaks is much more intense than the lower pair, so the anticorrelated quadruplet appears to be more similar to a typical exciton duplet (symmetric with respect to the diagonal). There are minor peaks with a lower degree of exciton mixing, *i.e.*, the exciton quadruplet $1-5$ ($P_{\text{coh}}(1,5) = 0.47$) and the exciton duplet $2-5$ ($P_{\text{coh}}(2,5) = 0.40$), oscillating with high frequencies (1214 and 709 cm^{-1}). There are also two minor purely vibrational quadruplets (due to $b = 2-3$ and $1-6$ coherences) oscillating at frequencies 245 and 1255 cm^{-1} corresponding (approximately) to $\Omega - 2M_{12}$ and $\Omega + 2M_{12}$.

We conclude that coupling to just a single vibration produces a manifold of coherent peaks of different physical nature (purely vibrational, exciton-vibrational, and predominantly excitonic) oscillating with different frequencies, depending on the disorder-induced shifts of the electronic transition energies.^{29,30} Thus, the 2D frequency map for any particular frequency may contain contributions from all (or at least many) vibrational modes coupled to the electronic transitions in a dimer. As a rough approximation we can collect all these contributions by calculating the 2D spectra of a dimer coupled to a single vibrational mode, and repeat this for a sequence of different vibrational frequencies. In such an approximation we neglect the effects produced by a combined action of many modes. However such a model allows the reproduction of the main features observed in 2D frequency maps, at frequencies that are below, near, and above the exciton resonance in the B820 dimer.

Modeling of 2D frequency maps

Now we switch to the modelling of the B820 experimental 2D frequency maps, obtained after Fourier transformation of the measured 2D spectra with respect to the population time. Fig. 5 shows the 2D maps at 345 , 416 , 546 , and 735 cm^{-1} oscillation frequencies together with the calculated maps. The calculated

data include all the components, *i.e.*, SE, ground-state bleaching (GSB) and excited-state absorption (ESA) averaged over disorder and over all possible orientations of the complex. Initial ground-state populations correspond to room temperature. In the excited state we restrict to coherent dynamics, *i.e.*, we do not consider the relaxation dynamics between different vibronic states. Without relaxation we cannot calculate the homogeneous broadening, so the line shapes are represented by some phenomenological line shapes. We consider the coupling to a single vibration, but its frequency is taken from the manifold of vibrational modes with frequencies $\Omega = \{195\ 345\ 416\ 546\ 735\ 970\ 1100\ 1360\ 1600\}$ cm^{-1} , and displacements $\Delta = \{0.51\ 0.86\ 0.43\ 0.46\ 0.83\ 0.63\ 0.67\ 0.66\ 0.69\}$. Note that in the single-mode model, the vibrational frequency should correspond to the oscillation frequency, *i.e.*, to reproduce the 2D map, for example at $345\ \text{cm}^{-1}$, we need to include the $345\ \text{cm}^{-1}$ vibration. Shifting of the vibrational frequency by a few cm^{-1} from $345\ \text{cm}^{-1}$ will result in some sizeable changes in the 2D map for the $345\ \text{cm}^{-1}$ oscillation frequency. The displacements of vibrational modes listed above correspond approximately to the shape of the MD/QC spectral density for the B850 α/β dimer,³¹ but we have increased the coupling for the 735, 970, and $1360\ \text{cm}^{-1}$ modes according to the Fourier amplitudes of the measured 2D kinetics. Note also that intense peaks near 735, 970, and $1360\ \text{cm}^{-1}$ are present in the measured spectral density for other complexes, for instance, for LHCII (see for a comparison of these spectral densities our modelling of bacterial LH2³²). After calculating the 2D spectra with contributions from all these frequencies (calculated sequentially and added) we perform a Fourier transformation of the resulting coherent dynamics and plot the 2D frequency maps for the 345, 416, 546, and $735\ \text{cm}^{-1}$ oscillation frequencies. Thus, the calculated 2D frequency maps are compared to the measured ones in Fig. 5. Notice that oscillations at any particular frequency, for example at $416\ \text{cm}^{-1}$, contain not only contributions from the original $416\ \text{cm}^{-1}$ vibrational mode but also contributions from mixed exciton-vibrational or pure exciton coherences produced by coupling to other modes (and oscillating at frequencies near $416\ \text{cm}^{-1}$ within a window of about 10 nm corresponding to phenomenological decay of the coherences that is supposed to be in the 0.5–1 ps range in our modeling). Thus, coupling to 970, 1100, 1360, and $1600\ \text{cm}^{-1}$ modes produces a lot of predominantly exciton coherences in the $400\text{--}550\ \text{cm}^{-1}$ region. Oscillations at $345\ \text{cm}^{-1}$ (that is lower than the exciton splitting) are determined mostly by vibrational coherences from the $345\ \text{cm}^{-1}$ mode and minor contributions from higher frequency modes. The structure of these minor contributions is illustrated by the low-frequency $245\ \text{cm}^{-1}$ vibrational quadruplet produced by the coupling of the exciton manifold to the $750\ \text{cm}^{-1}$ vibrational mode as shown in the bottom frame of Fig. 7.

At low frequencies ($345\ \text{cm}^{-1}$) the most intense peak is the diagonal vibrational one. At the frequencies near the exciton splitting (416 and $545\ \text{cm}^{-1}$) there are several components with significant exciton-type mixing that give symmetric off-diagonal peaks and some peaks shifted below the diagonal. Due to

exciton contributions the diagonal peak becomes less intense, whereas the peak below the diagonal becomes dominant (due to specific excitonic peaks shifted below the diagonal and also due to the cancelation of the excitonic SE and ESA components above the diagonal). At $735\ \text{cm}^{-1}$ there is still a significant contribution from the exciton peaks appearing in realizations with significant asymmetry of the two molecules (thus increasing the apparent splitting between exciton components up to $735\ \text{cm}^{-1}$). The average degree of exciton mixing P_{coh} is maximal for the off-diagonal peaks of the 2D frequency maps shown in Fig. 5, *i.e.*, $\langle P_{\text{coh}} \rangle = 0.21, 0.55, 0.63$, and 0.41 for the off-diagonal peaks of the 345, 416, 546, and $735\ \text{cm}^{-1}$ maps, respectively. For lower ($195\ \text{cm}^{-1}$) and higher ($970\ \text{cm}^{-1}$) frequencies the maximal $\langle P_{\text{coh}} \rangle$ value drops to 0.07 and 0.10, respectively. Thus, the relative increase of the amplitude of off-diagonal peaks, with respect to the diagonal peak, is a general feature reflecting the presence of exciton-type coherence. On the other hand, the amplitudes of the diagonal and off-diagonal peaks in the 2D frequency maps are very sensitive to the parameters of the model, in particular to the line shapes. We have found that predominantly vibrational coherence can produce 2D maps where the diagonal peak is the most intense or maps dominated by a peak below the diagonal, *i.e.*, appearing very similar to the exciton-type peaks. Therefore, the only possibility to fully distinguish between exciton and vibrational coherences is to perform a consistent fit of all the 2D kinetics or 2D Fourier-transformation maps at various frequencies. Such an analysis as performed here for the B820 complex allows us to reveal the simultaneous presence of different types of coherences, *i.e.*, pure vibrational, mixed exciton-vibrational coherence, and predominantly exciton coherence.

4 Discussion

2DES is a powerful tool to study both the static and the dynamic properties of the exciton manifold in photosynthetic pigment-protein complexes. Static features such as the spectral distribution of the excited state absorption band can be studied from the population time spectra as shown in Fig. 2. In fact 2DES, differently from transient absorption, is a selective technique, meaning that the excited state absorption (ESA) contribution to the signal is not necessarily superimposed on the ground state bleaching or on the stimulated emission contributions. However the 2D rephasing spectra also contain contributions from the intrinsic lineshape, therefore for the study of such features it is better to consider the total real spectra (see ESI†). The spectral distribution of ESA can be extrapolated from the spectra without any deconvolution, for example the (820,790) nm peak corresponds to ESA from the super-radiant state (see ESI†). This negative peak is centered at 790 nm with a broadening of about 40 nm (in the real total spectrum). This result is in full agreement with the spectral deconvolution of the transient absorption data.³³

The dynamics can be extrapolated from the T dependency of the traces and from the frequency maps. In the traces, the fact

that the oscillations last for more than 600 fs is a signature of vibrational or vibronic coherences. In fact, pure electronic coherences should de-phase in a few hundred femtoseconds.^{27,29} The frequencies in the power spectral density reported in Table 1 were previously found in transient absorption³⁴ and in 3 Photon Echo Peak Shift³⁵ experiments. These frequencies, which are between 100 and 750 cm⁻¹, reflect pure vibrational and mixed exciton-vibrational coherences. In the latter case the exciton interaction between the two sites does not create a significant mixing of the electronic states, but changes the shape of the excited-state potential surface, thus reducing the vibronic frequency. The exciton coherence contribution becomes significant for the oscillating peaks corresponding to frequencies near the exciton splitting value (400–550 cm⁻¹). Significant exciton coherences are also present at higher frequencies, *i.e.* up to 700–800 cm⁻¹, being determined by realizations of the disorder with a large energy gap between the two pigments (which increases the apparent value of the exciton splitting). Thus, in the region of 400–800 cm⁻¹ the exciton splitting can become resonant with the coherent vibrational motion (depending on the realization of the disorder), producing a non-trivial interplay between the vibrational and exciton degrees of freedom (accompanied by specific spectral signatures which appear in the linear absorption and in the 2D frequency maps). Our study of the B820 subunit demonstrates that coherence transfer occurring in a system with quasi-static conformational disorder and with coupling of exciton states to a manifold of vibrations, generally produces a rich dynamic picture with a variety of coherences varying from purely vibrational to mixed and to predominantly exciton coherences. Note that in the calculated frequency maps, the maximum averaged degree of exciton mixing ($\langle P_{\text{coh}} \rangle$) is 0.63, meaning that the long lasting oscillations are never due to pure exciton coherences. Assignment of these types of coherences is a challenging problem. We show that the frequency analysis and its representation in 2D frequency maps, in combination with modelling, provide a unique tool which gives new insights into this puzzle. Note that in this model the exciton manifold is coupled to different single vibrational modes, and the exciton-vibrational relaxation is neglected. However this relaxation most likely occurs on the timescale of the measurements and probably it will play a role in the dynamics of the coherences. In order to take into account the exciton-vibrational relaxation, the interaction with all the vibrational modes should be included in the model. This would allow the calculation of the homogeneous broadening and the corresponding decay rate of the coherences.

5 Experimental

Sample

The B820 dimer is prepared from the carotenoidless strain *R. rubrum* G9 as described elsewhere.²¹ Samples are in buffer containing 50 mM phosphate buffer pH 7.8, 1.3% β -OG, and 20% (v/v) glycerol.

Spectroscopy

2D electronic spectra are recorded at room temperature with a passively stabilized diffractive optics based set-up, which was described previously in detail.³⁶ Double modulation lock-in detection is used in order to reduce the noise and to enhance the sensitivity.³⁶ The coherence time (τ) is scanned from –70 fs to 120 fs, with a step of 1 fs. The population time (T) is scanned from 0 to 100 fs, with a 10 fs step, and from 100 fs to 700 fs with a 20 fs step, in addition, spectra at longer T (1 ps, 5 ps and 10 ps) are recorded. The laser system (PHAROS, Light Conversion) repetition rate is set to 1 kHz. The laser pulses are generated using a home-built non-collinear optical parametric amplifier (NOPA). Each pulse is centered at 820 nm with a full width half maximum (FWHM) of 90 nm in order to excite the Q_Y bands of the dimer, as is shown in Fig. 1. The pulse duration is 16 fs, the energy per pulse is 1 nJ and the spot diameter on the sample is 100 μ m.

6 Conclusions

The Fourier analysis of the 2D spectra in combination with modeling based on a two-pigment Hamiltonian in the basis of electronic and vibrational states is applied to study the nature of quantum coherences in the protein-bound BChl dimer B820, the basic unit of the bacterial light-harvesting complex LH1. We observe the simultaneous presence of different types of coherence, including pure vibrational, mixed exciton-vibrational and predominantly exciton coherences, that determine the complicated 2D-echo responses with long-lived oscillatory components over a wide range of frequencies (with the most intense components between 100 and 750 cm⁻¹). The resonance between vibrational modes and exciton states near the exciton splitting energy produces predominantly exciton coherence. In conclusion, we present the specific 2D frequency map features which are characteristic of pure vibrational, mixed exciton-vibrational and predominantly exciton coherences.

Differently from previous work we apply a Fourier analysis in combination with modelling which allows us to understand clearly the nature of quantum coherences in the B820 dimer. The understanding of these features is an essential tool aimed at assisting in the assignment of the nature and therefore the role and interplay of electronic and vibrational coherences in other photosynthetic complexes.

Acknowledgements

M.F., E. R. and R. v. G. were supported by the Royal Dutch Academy of Sciences (KNAW), the VU University Amsterdam, the TOP grant (700.58.305) from the Foundation of Chemical Sciences part of NWO and the advanced investigator grant (267333, PHOTPROT) from the European Research Council. M.F., E. R. and R. v. G. thank the support from the EU FP7 project PAPETS (GA 323901). V. I. N. was supported by the Russian Foundation for Basic Research (Grant No. 12-04-01085). R. A. and D. Z. acknowledge the support from the Swedish

Research Council, The Knut and Alice Wallenberg Foundation, Wenner-Gren Foundations and Crafoord Foundation.

Notes and references

- 1 R. van Grondelle, J. P. Dekker, T. Gillbro and V. Sundström, *Biochim. Biophys. Acta, Bioenerg.*, 1994, **1187**, 1–65.
- 2 G. R. Fleming and R. van Grondelle, *Phys. Today*, 1994, 48–55.
- 3 R. Van Grondelle and V. I. Novoderezhkin, *Phys. Chem. Chem. Phys.*, 2006, **8**, 793–807.
- 4 S. Savikhin, D. R. Buck and W. S. Struve, *Chem. Phys.*, 1997, **223**, 303–312.
- 5 G. S. Engel, T. R. Calhoun, E. L. Read, T.-K. Ahn, T. Mancal, Y.-C. Cheng, R. E. Blankenship and G. R. Fleming, *Nature*, 2007, **446**, 782–786.
- 6 E. Collini, C. Y. Wong, K. E. Wilk, P. M. G. Curmi, P. Brumer and G. D. Scholes, *Nature*, 2010, **463**, 644–647.
- 7 R. van Grondelle and V. I. Novoderezhkin, *Nature*, 2010, **463**, 614–615.
- 8 T. Brixner, J. Stenger, H. M. Vaswani, M. Cho, R. E. Blankenship and G. R. Fleming, *Nature*, 2005, **434**, 625–628.
- 9 D. Zigmantas, E. L. Read, T. Mancal, T. Brixner, A. T. Gardiner, R. J. Cogdell and G. R. Fleming, *Proc. Natl. Acad. Sci. U. S. A.*, 2006, **103**, 12672–12677.
- 10 Y.-C. Cheng and G. R. Fleming, *J. Phys. Chem. A*, 2008, **112**, 4254–4260.
- 11 N. Christensson, H. F. Kauffmann, T. Pullerits and T. Mančal, *J. Phys. Chem. B*, 2012, **116**, 7449–7454.
- 12 A. Kolli, E. J. O'Reilly, G. D. Scholes and A. Olaya-Castro, *J. Chem. Phys.*, 2012, **137**, 174109.
- 13 A. W. Chin, S. F. Huelga and M. B. Plenio, *Philos. Trans. R. Soc., A*, 2012, **370**, 3638–3657.
- 14 A. W. Chin, J. Prior, R. Rosenbach, F. Caycedo-Soler, S. F. Huelga and M. B. Plenio, *Nat. Phys.*, 2013, **9**, 113–118.
- 15 V. Tiwari, W. K. Peters and D. M. Jonas, *Proc. Natl. Acad. Sci. U. S. A.*, 2013, **110**, 1203–1208.
- 16 F. Fassioli, A. Olaya-Castro and G. D. Scholes, *J. Phys. Chem. Lett.*, 2012, **3**, 3136–3142.
- 17 H. Lee, Y.-C. Cheng and G. R. Fleming, *Science*, 2007, **316**, 1462–1465.
- 18 J. M. Womick and A. M. Moran, *J. Phys. Chem. B*, 2011, **115**, 1347–1356.
- 19 M. C. Chang, P. M. Callahan, P. S. Parkes-Loach, T. M. Cotton and P. A. Loach, *Biochemistry*, 1990, **29**, 421–429.
- 20 R. W. Visschers, M. C. Chang, F. van Mourik, P. S. Parkes-Loach, B. A. Heller, P. A. Loach and R. van Grondelle, *Biochemistry*, 1991, **30**, 5734–5742.
- 21 A. Pandit, R. W. Visschers, I. H. M. van Stokkum, R. Kraayenhof and R. van Grondelle, *Biochemistry*, 2001, **40**, 12913–12924.
- 22 R. Monshouwer, M. Abrahamsson, F. Van Mourik and R. Van Grondelle, *J. Phys. Chem. B*, 1997, **101**, 7241–7248.
- 23 A. W. Roszak, T. D. Howard, J. Southall, A. T. Gardiner, C. J. Law, N. W. Isaacs and R. J. Cogdell, *Science*, 2003, **302**, 1969–1972.
- 24 A. G. Yakovlev, M. R. Jones, J. A. Potter, P. K. Fyfe, V. G. Lyudmila, A. Y. Shkuropatov and V. A. Shuvalov, *Chem. Phys.*, 2005, **319**, 297–307.
- 25 V. I. Novoderezhkin, R. Monshouwer and R. van Grondelle, *J. Phys. Chem. B*, 1999, **103**, 10540–10548.
- 26 R. W. Visschers, F. van Mourik, R. Monshouwer and R. van Grondelle, *Biochim. Biophys. Acta, Bioenerg.*, 1993, **1141**, 238–244.
- 27 E. Romero, R. Augulis, V. I. Novoderezhkin, M. Ferretti, J. Thieme, D. Zigmantas, R. Van Grondelle, submitted.
- 28 V. I. Novoderezhkin, M. A. Palacios, H. van Amerongen and R. van Grondelle, *J. Phys. Chem. B*, 2004, **108**, 10363–10375.
- 29 V. Butkus, D. Zigmantas, D. Abramavicius and L. Valkunas, *Chem. Phys. Lett.*, 2013, **587**, 93–98.
- 30 V. Butkus, L. Valkunas, D. Abramavicius, *arXiv:1310.1343v2*, 2013.
- 31 A. Damjanović, I. Kosztin, U. Kleinekathöfer and K. Schulten, *Phys. Rev. E: Stat., Nonlinear, Soft Matter Phys.*, 2002, **65**, 031919.
- 32 V. I. Novoderezhkin, T. A. Cohen Stuart and R. van Grondelle, *J. Phys. Chem. A*, 2011, **115**, 3834–3844.
- 33 H. M. Visser, O. J. Somsen, F. van Mourik, S. Lin, I. H. van Stokkum and R. van Grondelle, *Biophys. J.*, 1995, **69**, 1083–1099.
- 34 W. M. Diffey, B. J. Homoele, M. D. Edington and W. F. Beck, *J. Phys. Chem. B*, 1998, **102**, 2776–2786.
- 35 J. Yu, Y. Nagasawa, R. van Grondelle and G. R. Fleming, *Chem. Phys. Lett.*, 1997, **280**, 404–410.
- 36 R. Augulis and D. Zigmantas, *Opt. Express*, 2011, **19**, 13126–13133.